Article

A Novel Hierarchical Recursive Nonsingular Terminal Sliding Mode Control for Inverted Pendulum

Hiep Dai Le * and Tamara Nestorović

Mechanics of Adaptive Systems Department, Ruhr-Universität Bochum, 44801 Bochum, Germany;
tamara.nestorovic@rub.de
* Correspondence: hiep.le-d9b@ruhr-uni-bochum.de

Abstract: This paper aims to develop a novel hierarchical recursive nonsingular terminal sliding mode controller (HRNTSMC), which is designed to stabilize the inverted pendulum (IP). In contrast to existing hierarchical sliding mode controllers (HSMC), the HRNTSMC significantly reduces the chattering problem in control input and improves the convergence speed of errors. In the HRNTSMC design, the IP system is first decoupled into pendulum and cart subsystems. Subsequently, a recursive nonsingular terminal sliding mode controller (RNTSMC) surface is devised for each subsystem to enhance the error convergence rate and attenuate chattering effects. Following this design, the HRNTSMC surface is constructed by the linear combination of the RNTSMC surfaces. Ultimately, the control law of the HRNTSMC is synthesized using the Lyapunov theorem to ensure that the system states converge to zero within a finite time. By invoking disturbances estimation, a linear extended state observer (LESO) is developed for the IP system. To validate the effectiveness, simulation results, including comparison with a conventional hierarchical sliding mode control (CHSMC) and a hierarchical nonsingular terminal sliding mode control (HNTSMC) are presented. These results clearly showcase the excellent performance of this approach, which is characterized by its strong robustness, fast convergence, high tracking accuracy, and reduced chattering in control input.

Keywords: adaptive sliding mode control; uncertainties; inverted pendulum; nonsingular terminal sliding mode; under-actuated system; hierarchical sliding mode

1. Introduction

The inverted pendulum (IP) system has been widely used in various industrial applications, such as balancing robots, rocket propellers, and humanoid robots [1–3], due to its cost-effectiveness and simple structure. However, the IP is an under-actuated system with fewer actuators than the degree of freedom to be controlled [4], which has strong nonlinearities, coupling properties, and is highly unstable [5]. Therefore, it provides many challenging problems with respect to linear and nonlinear control theories.

Since the 1950s, the IP has been employed as a platform for designing, evaluating, and comparing different control techniques [6]. Over the past decades, many controllers have been proposed for the IP to balance the pendulum at desired positions. One of the most straightforward controllers, a proportional–integral–derivative (PID) [7] controller, operates based on error values, which represent the difference between the actual values of the process and the desired ones. Thus, Ghosh [8] proposed the PID controllers to balance the IP at the desired cart position. This approach involved the use of two controllers: the first one for regulating the angular pendulum and the other for controlling the cart position. The robustness and performance of the PID controller were verified by simulations and practical experiments. However, a poorly tuned PID controller can drastically reduce system performance and lead to instability [9]. Thus, Wang [10] proposed a linear quadratic regulator (LQR) controller for the IP, with the response time and overshoot depending directly on the selection of the matrices **Q** and **R**. Although PID and LQR are known for their simple

structures and easy implementation, they usually fail to effectively reject disturbances [11] such as system parameter uncertainties, friction forces, unmodeled dynamics, vibration, wind forces, and unpredictable collisions. In practice, these disturbances are present in most systems and can significantly degrade the control performance. To address this issue, numerous nonlinear control methods have been developed, such as fuzzy design [12], neural networks [13], and sliding mode control (SMC) [14]. Their performance outcomess have been investigated for the IP system in Ref. [15]. The authors of that study noted that none of these single controllers could meet the best comparative criteria, including simplicity, fast response, precision, disturbances rejection, adaptability, robustness, tracking capabilities, and reduced chattering. Among these approaches, the SMC has been considered to be an effective controller for the IP due to its ability to provide fast responses, precision, disturbances rejection, adaptability, and tracking capabilities. Conventional sliding mode control (CSMC), which was first designed by Utkin [16], is based on high-speed switching control laws to drive the system trajectory to a selected sliding surface [17]. Once the system states reach the selected sliding surface, the system's response becomes insensitive to disturbances and parametric uncertainties. Thanks to this property, the CSMC has been employed in many applications such as missiles [18], piezos [19], and grippers [20]. Nevertheless, the CSMC is not without its limitations, including slow response and chattering. Achieving fast convergence with the CSMC often requires high control input, which can drive actuators to saturation. In response to these limitations, the terminal sliding mode control [21] (TSMC) was developed to attain finite convergence without using high-control input. Compared to the CSMC, the TSMC has gained popularity in robust control because of its faster time convergence and diminished steady-state errors. Nonetheless, the TSMC suffers two major drawbacks: firstly, it exhibits slower performance than the CSMC when system states are far from equilibrium points $e(t) = 0$; secondly, it faces a singularity problem in its control law. To address this issue, Yu [22] proposed the fast terminal sliding mode control (FTSMC), which can increase the error convergence while conquering the first drawback of the TSMC with a faster response. Despite these improvements, the control design still brings a singularity problem. Therefore, Feng [23] introduced the nonsingular terminal sliding mode control (NTSMC) to increase the convergence speed and avoid the singularity problem. Subsequently, Shao [24] combined the NTSMC with the integral sliding mode to enhance tracking performance outcomes and reduce steady-state errors in the IP. Besides the convergence speed problems, an inherent challenge in the SMC is the presence of chattering caused by the signum function. When the chattering occurs, the control input oscillates at a high frequency, thereby reducing the life of the actuators, degenerating the control accuracy, causing high wear and tear in mechanical parts, and generating high power losses in electrical circuits [25]. A possible method to reduce the level of chattering is using the smooth function instead of the signum function [26,27]. However, it compromises the control's smoothness and overall system performance. Another feasible solution is the integration of a disturbance observer in the control design. Thanks to its ability to rapidly reject disturbances, disturbance observer-based control design has been widely used as an effective method to compensate for the disturbances and uncertainties stemming from both the environment and system [28]. Therefore, combining the SMC with the disturbance observers is a promising approach because the SMC only needs to address the disturbance estimation errors [29,30]. A comprehensive review of these disturbance observers [31] revealed that the linear extended state observer (LESO) is the most commonly used technique for disturbance estimation without requiring accurate modeling [32]. Moreover, the simplicity of the design process and parameter adjustments make the LESO easily implementable in engineering applications such as motor drive systems [33] and exoskeletons [34].

In previous studies, the SMCs were typically investigated and demonstrated for the fully actuated system, thus making them useless for direct applications in under-actuated systems [35]. This challenge arises from the inability to directly calculate control parameters for a sliding mode surface using Hurwitz conditions [4]. To deal with this limitation,

Utkin [36] transformed the linearized equations of the system to regular forms and then employed them for SMC design. However, when the initial angular pendulum is far from an unstable equilibrium point, these control approaches may yield unsatisfactory results [37]. Another approach for designing the SMC without using a linear model for under-actuated systems is to use the SMC in a hierarchical structure, which not only retains the advantages of the SMC, but also has the ability to simultaneously control different outputs [38]. This method involves decoupling the under-actuated system into subsystems. For each subsystem, a sliding mode surface is meticulously designed based on the corresponding state system, thereby forming the initial level of a hierarchical structure. Then, the second level of the hierachical strucutere is constructed based on the first level. Finally, all the control laws of the different subsystems are interconnected to form the ultimate control law. By implementing this method, the high-dimensional system is effectively reduced to lower-dimensional subsystems, thereby reducing the complexity of the controller design. The conventional hierarchical sliding mode control (CHSMC) [39–42] was proposed for underactuated systems by using the CSMC in a hierarchical form. These results proved the effectiveness of the CHSMC controller for tracking the cart position while balancing the pendulum. However, using the CSMC to design the CHSMC leads to slow error convergences. Although adjusting controller coefficients can increase the error convergence speed, the errors of the sliding surface can not converge to equilibrium in a finite time. In response to this challenge, Refs. [43,44] designed the hierarchical nonsingular terminal sliding mode control (HNTSMC) for the IP to increase the error convergence speed. Nevertheless, these control laws contain signum structures that are premultiplied by the bound of the lumped disturbances, which means that chattering is not effectively reduced [45].

As aforementioned, both the CHSMC and the HNTSMC suffer from chattering problems in the control input and lack results related to the disturbance observer for the IP system. To the best of our knowledge, there is no research in the literature regarding the development of a hierarchical recursive nonsingular terminal sliding mode controller (HRNTSMC) for the IP. Compared to existing results, the main advantages of the proposed controller can be outlined as follows: (1) A new HRNTSMC has been introduced to the IP for reducing chattering phenomena in the control input, thereby increasing the error convergence speed and saving energy consumption. The RNTSMC has been developed for each subsystem, including the integration of the NTSMC to enhance the convergence and tracking precision of the subsystem states [46]. Compared to the CHSMC and HNTSMC, the proposed controller demonstrated better performance when the IP suffered from more lumped disturbances and high initial errors of angular pendulum; (2) The disturbances of the IP were directly estimated by using the LESO, that is, the proposed controller compensated for these disturbances with more accuracy and efficiency; (3) The reaching law of the proposed controller compensated the estimation errors of the LESO results with respect to chattering reduction in the control input; (4) The overall stability of the control system was analyzed using the Lyapunov theorem. The proposed controller can extend to a general under-actuated system with input coupling.

The remainder of the article is organized as follows: Section 2 formulates the problem associated with the IP. Section 3 provides a comprehensive description of the proposed controller and system stability. Section 4 presents the results of numerical simulations for the IP. Finally, Section 5 draws some conclusions and outlines potential directions for future works.

2. Problem Formulation

The IP in Figure 1 is considered to be the most exemplary laboratory experiment to perform nonlinear control techniques. It comprises a cart moving along a guiding rail and an aluminium rod mounted on a cart, thereby allowing the rod to freely swing within a vertical plane. The cart is moved by a DC motor connected via a belt. The dynamic model

of the IP (Figure 1) is derived using the Lagrange equation according to the following set of equations [47]:

$$\dot{x}_1(t) = x_2(t), \tag{1}$$

$$\dot{x}_2(t) = f_1(\mathbf{x}, t) + b_1(\mathbf{x}, t)u(t) + n_1(t), \tag{2}$$

$$\dot{x}_3(t) = x_4(t), \tag{3}$$

$$\dot{x}_4(t) = f_2(\mathbf{x}, t) + b_2(\mathbf{x}, t)u(t) + n_2(t), \tag{4}$$

where $f_1(\mathbf{x}, t), b_1(\mathbf{x}, t), f_2(\mathbf{x}, t), b_2(\mathbf{x}, t)$ are given as

$$f_1(\mathbf{x}, t) = \frac{m_t g sin(x_1(t)) - m_p L sin(x_1(t)) cos(x_1(t)) x_2(t)^2}{L(4/3m_t - m_p cos^2(x_1(t)))}, \tag{5}$$

$$b_1(\mathbf{x}, t) = \frac{cos(x_1(t))}{L(4/3m_t - m_p cos^2(x_1(t)))}, \tag{6}$$

$$f_2(\mathbf{x}, t) = \frac{-4/3m_p L x(t)_2^2 sin(x_1(t)) + m_p g sin(x_1(t)) cos(x_1(t))}{4/3m_t - m_p cos^2(x_1(t))}, \tag{7}$$

$$b_2(\mathbf{x}, t) = \frac{4}{3(4/3m_t - m_p cos^2(x_1(t)))}, \tag{8}$$

where the system state vector $\mathbf{x} = [x_1, x_2, x_3, x_4]^T$, $x_1(t)$ is the angular position of the pendulum from the vertical axis; $x_2(t)$ is the angular velocity of the pendulum; $x_3(t)$ is the position of the cart; $x_4(t)$ is the velocity of the cart; m_t is the total mass (in kg) of the cart mass m_c and pendulum mass m_p; L is the half-length of the pendulum (in m); g is the acceleration of gravity (in m/s^2); $u(t)$ is the force applied to the cart (N); and $n_1(t)$ and $n_2(t)$ are lumped disturbances, which include the uncertainties and external disturbances of the system.
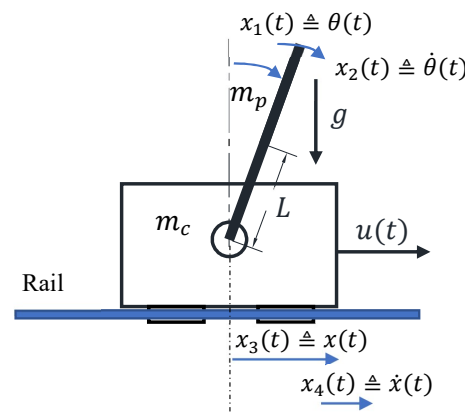

Figure 1. The mechanical model of the IP.

Assumption 1. *The unknown lumped disturbances of the system and its first time derivatives are bounded [48], with the specific bounds being unknown. This assumption represents all of the continuous and bounded disturbances, including but not limited to constant disturbances, harmonic disturbances, or neutral stable disturbances, thereby representing various disturbances in engineering applications.*

Remark 1. *When deriving a mathematical model, it is necessary to take into account the accuracy of the system model. However, a highly accurate model may comprise several terms, which can be cumbersome to determine. Therefore, in this work, the authors did not consider friction forces, including viscous, coulomb, and static (dry) friction forces, which can make the IP model more complex. Instead, these forces were assumed as parts of the lumped disturbance.*

Remark 2. *The actuator in the IP, consisting of a DC motor with a gearbox, is regarded as a subsystem of the IP model. While this dynamic can be neglected by comparing it with the dynamics of the IP, it is important to recognize that the actuator's dynamic can significantly affect the overall performance of the control system. This problem can be solved by implementing an internal control system, such as an open-loop proportional regulator or a PID controller, to control the DC motor [49].*

Remark 3. *Based on the system model (1)–(4), the same control input $u(t)$ appears in two dynamic equations. Therefore, the whole system is under-actuated (single input multioutput).*

Definition 1. *The detailed expressions of the notation $sig(e)^\alpha$ can be found in [50], which can be expressed as follows:*

$$sig(e)^\alpha = |e|^\alpha sgn(e), \tag{9}$$

where $\alpha > 0 \forall e \in \mathbb{R}$. Note that the function $sig(e)^\alpha$ is smooth and monotonically increasing.

The objective of this work is to propose a new hierarchical sliding mode controller that can navigate the cart to desired positions while balancing the pendulum on its upright position with minimal deflection in the presence of disturbances and uncertainties.

3. Control Strategy and Stability Analysis

The proposed controller (Figure 2) comprises a hierarchical structure and an LESO observer. The hierarchical structure uses the RNTSMC for the first level of the structure. The LESO is utilized to observe the lumped disturbance of each subsystem. Afterwards, the reaching law is applied to compensate for the approximation errors of the LESO.
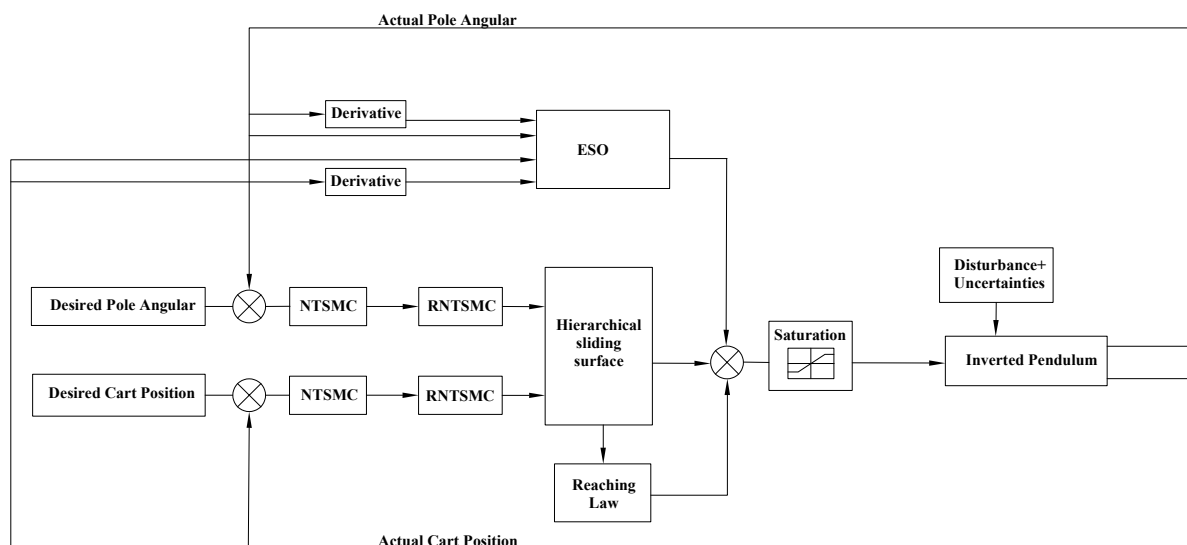

Figure 2. The structure of proposed control.

3.1. Design Hierarchical Recursive Nonsingular Terminal Sliding Mode Control

According to the dynamic model of the IP, the hierarchical structure in Figure 3 is employed to design controllers for the two subsystems [51]. The first subsystem is the pendulum, which has state variables $[x_1(t), x_2(t)]$, and the second is the cart, which includes state variables $[x_3(t), x_4(t)]$. The first layer of the hierarchical structure comprises the sliding mode surface of each subsystem: the subsystem sliding surface $\sigma_1(t)$ and the

subsystem sliding surface $\sigma_2(t)$. The second layer of the hierarchical structure comprises sliding mode surfaces in the first layer. The total control law is synthesized from the hierarchical structure by employing the Lyapunov theory, thereby ensuring the stability of each sliding surface within the subsystem.
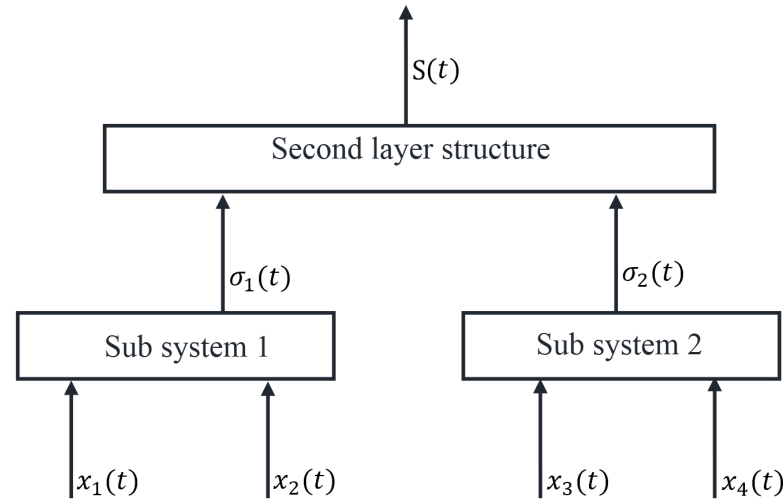

Figure 3. Hierarchical structure is given by [51].

The error of the angular pendulum is defined as follows:

$$e_1(t) \triangleq x_1(t) - x_{1d}(t), \tag{10}$$

where $x_1(t)$ is the actual angle of the pendulum, and $x_{1d}(t)$ is the desired angle of the pendulum. In addition, we define the error of the cart position as follows:

$$e_3(t) \triangleq x_3(t) - x_{3d}(t), \tag{11}$$

where $x_3(t)$ is the actual position of the cart, and $x_{3d}(t)$ is the desired position of the cart.

The NTSMC surface was presented by [24], who adapted for the first subsystem (1) and (2) as follows:

$$s_1(t) \triangleq \dot{e}_1(t) + k_1 e_1(t) + \gamma_1 sig(e_1(t))^{r_1}, \tag{12}$$

where $r_1 > 1$; $\gamma_1 > 0$; and $k_1 > 0$ are the control parameters to be designed. Then, the RNTSMC surface $\sigma_1(t)$ for the first subsystem is defined as follows:

$$\sigma_1(t) \triangleq s_1(t) + \gamma_2 \int_0^t sig(s_1(t))^{r_2}, \tag{13}$$

where the control parameters are $1 > r_2 > 0$ and $\gamma_2 > 0$ [52], and the variable $s_1(t)$ is defined in (12).

The first time derivative of (13) becomes the following:

$$\dot{\sigma}_1(t) = \dot{s}_1(t) + \gamma_2 sig(s_1(t))^{r_2}, \tag{14}$$

where the time derivative of $s_1(t)$ is defined as follows:

$$\dot{s}_1(t) = f_1(\mathbf{x}, t) + b_1(\mathbf{x}, t)u(t) + n_1(t) - \ddot{x}_{1d}(t) + k_1 \dot{e}_1(t) + \gamma_1 r_1 |e_1(t)|^{r_1 - 1} \dot{e}_1(t). \tag{15}$$

The NTSMC surface for the second subsystem (3) and (4) is described as follows:

$$s_2(t) \triangleq \dot{e}_3(t) + k_2 e_3(t) + \gamma_3 sig(e_3(t))^{r_3}, \tag{16}$$

where the design parameters are set as $r_3 > 1$; $\gamma_3 > 0$; and $k_2 > 0$.

We introduce the RNTSMC surface $\sigma_2(t)$ for the second subsystem as follows:

$$\sigma_2(t) \triangleq s_2(t) + \gamma_4 \int_0^t sig(s_2(t))^{r_4}, \tag{17}$$

where $1 > r_4 > 0$ and $\gamma_4 > 0$ are the design parameters.

Differentiating (17) with respect to time yields the following:

$$\dot{\sigma}_2(t) = \dot{s}_2(t) + \gamma_4 sig(s_2(t))^{r_4}, \tag{18}$$

where

$$\dot{s}_2(t) = f_2(\mathbf{x}, t) + b_2(\mathbf{x}, t)u(t) + n_2(t) - \ddot{x}_{3d}(t) + k_2\dot{e}_3(t) + \gamma_3 r_2 |e_3(t)|^{r_2-1}\dot{e}_3(t). \tag{19}$$

The second-level hierarchical structure based on the first level is defined as follows:

$$S(t) \triangleq \alpha\sigma_1(t) + \sigma_2(t), \tag{20}$$

where α is a positive or negative design constant, and $\sigma_1(t)$ and $\sigma_2(t)$ are defined, respectively, in (13) and (17).

Differentiating $S(t)$ with respect to time yields the following:

$$\dot{S}(t) = \alpha\dot{\sigma}_1(t) + \dot{\sigma}_2(t). \tag{21}$$

Based on (14) and (18), let $\dot{\sigma}_1(t) = 0$ and $\dot{\sigma}_2(t) = 0$; the equivalent control laws $u_{1eq}(t)$ and $u_{2eq}(t)$ can be obtained for the corresponding subsystems as follows:

$$u_{1eq}(t) = -1/b_1(\mathbf{x}, t)(f_1(\mathbf{x}, t) + n_1(t) - \ddot{x}_{1d}(t) + k_1\dot{e}_1(t) + \gamma_1 r_1|e_1(t)|^{r_1-1}\dot{e}_1(t) \\ +\gamma_2 sig(s_1(t))^{r_2}). \tag{22}$$

$$u_{2eq}(t) = -1/b_2(\mathbf{x}, t)(f_2(\mathbf{x}, t) + n_2(t) - \ddot{x}_{3d}(t) + k_2\dot{e}_3(t) + \gamma_3 r_3|e_1(t)|^{r_3-1}\dot{e}_1(t) \\ +\gamma_4 sig(s_2(t))^{r_4}). \tag{23}$$

A constant plus the proportion reaching law [53] $\dot{S}(t) = -\kappa_1 S(t) - \kappa_2 sign(S(t))$ are employed to design this controller, where $\kappa_1 > 0$ is the switching gain; $\kappa_2 > 0$ is the reaching control gain; and $sign(S(t))$ is the signum function defined as the form:

$$sign(S(t)) = \begin{cases} 1 & \text{if } S(t) > 0, \\ 0 & \text{if } S(t) = 0, \\ -1 & \text{if } S(t) < 0. \end{cases}$$

Based on [54,55], the total control law is determined as follows:

$$u(t) \triangleq \frac{\alpha b_1(\mathbf{x}, t)u_{1eq}(t) + b_2(\mathbf{x}, t)u_{2eq}(t) - \kappa_1 S(t) - \kappa_2 sign(S(t))}{\alpha b_1(\mathbf{x}, t) + b_2(\mathbf{x}, t)}. \tag{24}$$

$$u_{eq}(t) \triangleq \frac{\alpha b_1(\mathbf{x}, t)u_{1eq}(t) + b_2(\mathbf{x}, t)u_{2eq}(t)}{\alpha b_1(\mathbf{x}, t) + b_2(\mathbf{x}, t)}. \tag{25}$$

$$u_{sw}(t) \triangleq \frac{-\kappa_1 S(t) - \kappa_2 sign(S(t))}{\alpha b_1(\mathbf{x}, t) + b_2(\mathbf{x}, t)}. \tag{26}$$

The proposed control law $u(t)$ from (24) consists of $u_{eq}(t)$ and $u_{sw}(t)$, which are mentioned later.

To demonstrate the stability analysis of the second-level hierarchical structure, we choose a Lyapunov function candidate as follows:

$$V(t) \triangleq \frac{1}{2}S(t)^2. \tag{27}$$

The time derivative of the Lyapunov function is thus obtained from the following:

$$\dot{V}(t) = S(t)\dot{S}(t) = S(t)(\alpha\dot{\sigma}_1(t) + \dot{\sigma}_2(t)). \tag{28}$$

$$
\begin{aligned}
\dot{V}(t) = S(t)\dot{S}(t) = S(t)(\alpha(f_1(\mathbf{x},t) + b_1(\mathbf{x},t)u(t) + n_1(t) - \ddot{x}_{1d}(t) \\
+ k_1\dot{e}_1(t) + \gamma_1 r_1|e_1(t)|^{r_1-1}\dot{e}_1(t) + \gamma_2 sig(s_1(t))^{r_2}) \\
+ (f_2(\mathbf{x},t) + b_2(\mathbf{x},t)u(t) + n_2(t) - \ddot{x}_{3d}(t) \\
+ k_2\dot{e}_3(t) + \gamma_3 r_2|e_3(t)|^{r_2-1}\dot{e}_3(t) + \gamma_4 sig(s_2(t))^{r_4})).
\end{aligned} \tag{29}
$$

We substitute (24) into (29) to yield the following:

$$\dot{V}(t) = S(t)(-\kappa_1 S(t) - \kappa_2 sign(S(t))). \tag{30}$$

$$\dot{V}(t) = -\kappa_1 S(t)^2 - \kappa_2|S(t)| < 0. \tag{31}$$

Therefore, $S(t)$ will converge to zero in finite time [56]. $\sigma_1(t)$ and $\sigma_2(t)$ will converge asymptotically to zero [4]. Then, the errors $e_1(t)$ and $e_3(t)$ converge to zero in finite time [24].

3.2. Design of Extended State Observer

The equivalent control $u_{1eq}(t)$ and $u_{2eq}(t)$ involves the knowledge of the lumped disturbances $n_1(t)$ and $n_2(t)$, which can be measured using intrinsic sensors. To estimate the knowledge of the lumped disturbances, the LESO [31] is employed for the IP system. The LESO, designed to estimate $n_1(t)$, is expressed as follows:

$$\varepsilon_1(t) \triangleq x_1(t) - \hat{x}_1(t), \tag{32}$$

$$\dot{\hat{x}}_1(t) \triangleq \hat{x}_2(t) + \frac{a_1\varepsilon_1}{\xi_1}, \tag{33}$$

$$\dot{\hat{x}}_2(t) \triangleq f_1(\mathbf{x},t) + b_1(\mathbf{x},t)u(t) + \hat{n}_1(t) + \frac{a_2\varepsilon_1(t)}{\xi_1^2}, \tag{34}$$

$$\hat{n}_1(t) \triangleq \frac{a_3\varepsilon_1(t)}{\xi_1^3}, \tag{35}$$

where $\xi_1 > 0$; a_1, a_2, and a_3 are positive constants, and the polynomial $s^3 + a_1s^2 + a_2s + a_3$ is Hurwitz; $\hat{x}_1(t), \hat{x}_2(t)$, and $\hat{n}_1(t)$ are the observed values of $x_1(t), x_2(t)$, and $n_1(t)$, respectively.

Proof. The proof is detailed in Appendix A. □

Remark 4. *The selection of the LESO parameters has a significant effect on the observer's stability, as has been thoroughly described in [57]. The estimation states from (32)–(34) depend on the error between the measured and the estimated angular pendulum. However, when the position error $e_1(t)$ becomes small, it is necessary to select the high gains in (33)–(35) to achieve a reliable estimation of the lump disturbances. Therefore, to achieve an accurate estimation of the lump disturbances, it is advisable to select larger values for the parameters $\frac{a_1}{\xi_1}, \frac{a_2}{\xi_1}$, and $\frac{a_3}{\xi_1}$. In practical implementation, the initial observation errors are usually nonzero due to the difference between the initial value of the LESO and the plant. Since the system employs a small ξ_1, the initial peak values of the LESO*

can become relatively large. This can lead to a significant demand for control force, which, in turn, potentially damages the motor, degrades the overall control performance, and negatively affects the observer's convergence. To alleviate the peaking phenomenon, ξ_1 is selected as follows [58,59]:

$$\frac{1}{\xi_1} = R = \begin{cases} 10t^3, 0 \le t \le 1, \\ 10, t > 1. \end{cases} \tag{36}$$

The LESO, designed to estimate $n_2(t)$, is expressed as follows:

$$\varepsilon_2(t) \triangleq x_3(t) - \hat{x}_3(t), \tag{37}$$

$$\hat{x}_3(t) \triangleq \hat{x}_4(t) + \frac{a_4\varepsilon_2(t)}{\xi_2}, \tag{38}$$

$$\hat{x}_4(t) \triangleq f_2(x,t) + b_2(x,t)u(t) + \hat{n}_2(t) + \frac{a_5\varepsilon_2(t)}{\xi_2^2}, \tag{39}$$

$$\hat{n}_2(t) \triangleq \frac{a_6\varepsilon_2(t)}{\xi_2^3}, \tag{40}$$

where $a_4, a_5,$ and a_6 are positive constants, and the polynomial $s^3 + a_4s^2 + a_5s + a_6$ is Hurwitz; $\hat{x}_3, \hat{x}_4,$ and $\hat{n}_2$ are the observed values of $x_1, x_2,$ and n_2, respectively; ξ_2 is selected based on (36).

Proof. The proof is similar to Appendix A. □

Based on (32) to (40), the lumped disturbances $n_1(t)$ and $n_2(t)$ are estimated by $\hat{n}_1(t)$ and $\hat{n}_2(t)$, respectively. We substitute $\hat{n}_1(t)$ and $\hat{n}_2(t)$ into (22) and (23), respectively; the equivalent controls $u_{1eq}(t)$ and $u_{2eq}(t)$ are then rewritten as follows:

$$u_{1eq}(t) = -1/b_1(\mathbf{x},t)(f_1(\mathbf{x},t) + \hat{n}_1(t) - \ddot{x}_{1d}(t) + k_1\dot{e}_1(t) + \gamma_1 r_1 |e_1(t)|^{r_1-1}\dot{e}_1(t) \\ + \gamma_2 sig(s_1(t))^{r_2}). \tag{41}$$

$$u_{2eq}(t) = -1/b_2(\mathbf{x},t)(f_2(\mathbf{x},t) + \hat{n}_2(t) - \ddot{x}_{3d}(t) + k_2\dot{e}_3(t) + \gamma_3 r_3 |e_1(t)|^{r_3-1}\dot{e}_1(t) \\ + \gamma_4 sig(s_2(t))^{r_4}). \tag{42}$$

To demonstrate the stability of the proposed controller, the Lyapunov is selected as follows:

$$V_2(t) \triangleq \frac{1}{2}S(t)^2. \tag{43}$$

Taking the time derivative of the Lyapunov function, one can obtain the following:

$$\dot{V}_2(t) = S(t)\dot{S}(t) = S(t)(\alpha\dot{\sigma}_1(t) + \dot{\sigma}_2(t)). \tag{44}$$

$$\dot{V}_2(t) = S(t)\dot{S}(t) = S(t)(\alpha(f_1(\mathbf{x},t) + b_1(\mathbf{x},t)u(t) + n_1(t) - \ddot{x}_{1d} \\ + k_1\dot{e}_1(t) + \gamma_1 r_1 |e_1(t)|^{r_1-1}\dot{e}_1(t) + \gamma_2 sig(s_1(t))^{r_2}) \\ + (f_2(\mathbf{x},t) + b_2(\mathbf{x},t)u(t) + n_2(t) - \ddot{x}_{3d}(t) \\ + k_2\dot{e}_3(t) + \gamma_3 r_2 |e_3(t)|^{r_2-1}\dot{e}_3(t) + \gamma_4 sig(s_2(t))^{r_4})). \tag{45}$$

We denote the estimation errors of $n_1(t)$ and $n_2(t)$ as follows:

$$\tilde{n}_1(t) \triangleq \hat{n}_1(t) - n_1(t), \tag{46}$$

$$\tilde{n}_2(t) \triangleq \hat{n}_2(t) - n_2(t). \tag{47}$$

We substitute (24) with the new equivalent control laws (41) and (42) into (45), which yields the following:

$$\dot{V}_2(t) = S(t)(-\kappa_1 S(t) - \kappa_2 sign(S(t)) + \alpha \tilde{n}_1(t) + \tilde{n}_2(t)). \tag{48}$$

$$\dot{V}_2(t) = -\kappa_1 S(t)^2 - \kappa_2|S(t)| + S(t)(\alpha \tilde{n}_1(t) + \tilde{n}_2(t)). \tag{49}$$

$$\dot{V}_2(t) < -\kappa_1 S(t)^2 - \kappa_2|S(t)| + |S(t)|(|\alpha \tilde{n}_1(t)| + |\tilde{n}_2(t)|). \tag{50}$$

κ_2 is selected as follows:

$$\kappa_2 > |\alpha \tilde{n}_1(t)| + |\tilde{n}_2(t)| + \kappa_3, \tag{51}$$

where κ_3 is a small positive number. Substituting (51) into (50) yields the following:

$$\dot{V}_2(t) < -\kappa_1 S(t)^2 - \kappa_3|S(t)| < 0. \tag{52}$$

$$\dot{V}_2(t) < -2\kappa_1 V_2(t) - \kappa_3\sqrt{2}V_2(t)^{1/2}. \tag{53}$$

Therefore, $S(t)$ will converge to zero in finite time:

$$T \le \frac{1}{\kappa_1}ln\frac{2\kappa_1 V_2^{1/2}(0) + \sqrt{2}\kappa_3}{\sqrt{2}\kappa_3}. \tag{54}$$

Then, $\sigma_1(t)$ and $\sigma_2(t)$ will converge asymptotically to zero [4], and the errors $e_1(t)$ and $e_3(t)$ converge to zero in finite time [24].

Remark 5. *The proposed control law $u(t)$ of (24) consists of two main components: $u_{eq}(t)$ and $u_{sw}(t)$. While $u_{eq}(t)$ is responsible for compensating the nominal parts, $u_{sw}(t)$ is designed to compensate for the impact of the estimation errors stemming from the LESO. The RNTSMC is designed for each subsystem, thus inheriting the merits of both the NTSMC and the high-order sliding mode control (HOSMC) [60] and ensuring finite time convergence and attenuated chattering.*

Remark 6. *The chattering of the proposed controller is significantly reduced by using the LESO, as it solely addresses the estimation errors of the lumped disturbances through the switching function (26) [61]. Despite its advantages, in practical scenarios, it is challenging to achieve a complete reduction of s to zero due to some factors such as noise, delay, and imperfection of the devices [62]. Consequently, the $sign(s)$ function in the control input is often substituted by the saturation to reduce the chattering effect. The sat function is given as follows [63]:*

$$sat(s) \triangleq \begin{cases} 1, s > \Delta, \\ ks, |s| \le \Delta, k = \frac{1}{\Delta}, \\ -1, s < -\Delta. \end{cases} \tag{55}$$

Remark 7. *In practical application, the control input (24) cannot be applied directly to the DC motor. Instead, some experiments are conducted to determine the relationship between the pulse-width-modulated (PWM) input duty and the rotation speed of the motor. Subsequently, the relationship between the rotation speed and the force output of the motor is determined by using catalog information and a wheel radius. Afterward, the required PWM duty can be calculated and provided to the DC motor to achieve the desired control input (24).*

3.3. Parameters Selection

The selection of the control parameters is of great importance for practitioners in practical implementation. The control performance can be compromised by factors such as control saturation, measurement noise, and chattering in the control signal. When choosing

parameters, it is essential to adhere to two fundamental rules: 1. Ensure that the conditions (12), (13), (16), (17), and (26) are satisfied in the designed controller. 2. Strive to keep the parameter values as small as possible to reduce the required force of the actuator.

Selecting the parameters of the sliding surfaces can be referred in Ref. [24]. In addition, the LESO parameters should align with the recommendation presented in Ref. [64]:

Selection of k_1, γ_1, and r_1: The parameters k_1, γ_1, and r_1 have a direct effect on the dynamic behaviours of the sliding surface (12). An increased value of these parameters leads to faster convergence of $e_1(t)$, but this comes at the expense of higher demand for the control input.

Selection of γ_2 and r_2: A larger γ_2 or r_2 will increase the convergent speed of the error $e_1(t)$ and reduce the steady-state tracking errors but at the cost of an increased control input requirement.

Selection of κ_1 and κ_2: These control parameters affect the robustness of the controller in (26). Higher values of these parameters improve the robustness but may lead to a less smooth control signal.

Selection of a_1, a_2, and a_3 : These parameters can be determined using Equation (A19), which solely requires the value of ω. A higher value of ω improves the accuracy of the disturbances estimation. However, it is worth noticing that if the measurement signal contains noise, substantial observer errors may arise when dealing with large ω values.

Remark 8. *The HRNTSMC surface can be considered as a general form encompassing both the CHSMC surface and HNTSMC surface. When $k_1 = 0, r_1 = 1$, and $\gamma_2 = 0$, the HRNTSMC surface is the same as the CHSMC surface. When $k_1 = 0, 2 > r_1 > 1$, and $\gamma_2 = 0$, the HRNTSMC surface exhibits similar behavior to the HNTSMC surface. The control parameters for the simulation results were tuned as follows: Initially, all the control parameters of the proposed controller were set to zero values. Subsequently, the values of γ_1 and κ_2 were adjusted, and r_1 was fixed at one, which made the proposed controller similar to the CHSMC [65]. Following that, we gradually increased the control parameters γ_1 and κ_2 to reach the optimal performance of the CHSMC, with an emphasis on minimizing the values of κ_2 to reduce chattering in the control input and maximizing γ_1 to increase the convergence speed of the errors. Afterwards, we selected r_1 in the range (1–2) while adjusting γ_1 to improve the convergence errors of the proposed controller. Following most related works of the NTSMC, r_1 was fixed at 5/3. To enhance the reaching phase speed of the proposed control, the values of κ_1 were increased, while those of κ_2 were adjusted. It is important to note that the values of κ_1 should be large to increase the reaching speed, whereas the values of κ_2 should be kept small to reduce the chattering. At this point, the proposed controller shares the same structure with the HNTSMC [43], which gains a fast convergence speed. However, since the control input suffers from more chattering, and there is a need for improved convergence speed, the remaining control parameters should be tuned to obtain the merit properties for the proposed controller. To accomplish this, the value ξ_1 of the LESO was set according to (36), and the values of ω in (A19) were selected to determine a_1, a_2, and a_3 for the LESO. Adjusting the ω values is essential to achieve satisfactory disturbance estimations while simultaneously reducing the values of κ_2 as much as possible. Additionally, gradually adjusting γ_2, r_2, and k_1 from small to large values in the proposed controller contributes to an improvement in both the convergence speed and accuracy.*

Remark 9. *The versatility of the proposed controller allows for its widespread applicability in other under-actuated systems such as acrobot, pendubot, magnetic suspension, beam-and-ball, and the TORA system. However, the proposed controller has more parameters for tuning to gain the optimal performance, which could be the limitation of this approach. Therefore, future work endeavors are expected to employ an optimization algorithm to identify the most suitable control parameters. In this work, the LESO has been successfully employed to estimate the lumped disturbances, which were assumed to be constant or low-frequency disturbances. However, a limitation in performance will arise when dealing with high-frequency disturbances. Therefore, a generalized integrator extended state observer [66] will be taken into consideration to estimate both slow and rapid disturbances in future work.*

3.4. Detailed Step for Designing Proposed Controller

The design procedures are summarized as follows:

Step 1: Initialize the control parameters and system states.

Step 2: Design sliding surfaces for two subsystems (13) and (17).

Step 3: Design the observers to determine $\hat{n}_1$ as in (32)–(35) and $\hat{n}_2$ as in (37)–(40).

Step 4: Determine the equivalent control laws in (41) and (42).

Step 5: Obtain the control input for the motor (24).

4. Simulation Verification

This section presents several simulation results to demonstrate the effectiveness of the proposed controller with respect to tracking errors, energy consumption, and chattering reduction. A comparative analysis was conducted between the proposed controller HRNTSMC and two existing controllers: the HNTSMC in [43] and the CHSMC in [65]. The CHSMC, which is characterized by its simplicity and feasibility, has been widely designed for under-actuated systems. Meanwhile, the HNTSMC not only inherits the characteristics of the CHSMC, but also ensures the faster convergence rate of system states to zero in finite time. The control systems were simulated in the MATLAB SIMULINK environment using the ODE 45 solver with a fixed step size of 0.001 s.

4.1. Simulation Condition

In the IP system, the system parameters were chosen as g = 9.8 m/s^2; m_t = 0.8 kg; m_p = 0.188 kg; and L = 0.34 m. In the first and second case, the initial conditions of the IP were set as follows: $[x_1 \, x_2 \, x_3 \, x_4]$ = $[\frac{-\pi}{15} \, 0 \, 0 \, 0]$; the initial conditions in the third case of the IP were set as $[x_1 \, x_2 \, x_3 \, x_4]$ = $[\frac{-\pi}{3} \, 0 \, 0 \, 0]$. The third case was designed to perform the advantage of the HRNTSMC over the other linear controllers, thus showcasing its ability to balance the IP even when starting from a large initial error of angular pendulum. The desired angle and position were obtained from [67,68] and were respectively defined as follows: $x_{1d} = 0$ rad and $x_{3d} = 0$ m.

The lumped disturbances of the pendulum and cart were assumed as follows [68]:

$$n_1(t) = 0.0873sin(t) + 0.5sin(x_1(t)); \tag{56}$$

$$n_2(t) = 0.0873sin(t) + 0.5sin(x_3(t)); \tag{57}$$

4.2. Simulation Results

It is worth noticing that the CHSMC, HNTSMC, and HRNTSMC use the same system parameters, initial conditions, and other common parameters [69]. The magnitude force was restricted to be less than 30 N [70]. The corresponding parameters of the different control systems were set with the same values [71,72]. The parameters of the controllers used in the first and second case are given in Table 1, while Table 2 shows the control parameters for the third case.

Table 1. Parameter settings of each controller for the first case and the second case.

Controller	Tuning Parameters
CHSMC	$\gamma_1 = 3; \gamma_3 = \gamma_1; \alpha = -2; \kappa_2 = 0.5$
HNTSMC	$\gamma_1 = 3; r_1 = 5/3; \gamma_3 = \gamma_1; r_3 = r_1; \alpha = -2; \kappa_1 = 2; \kappa_2 = 1$
HRNTSMC	$k_1 = 2; \gamma_1 = 3; r_1 = 5/3; \gamma_2 = 2; r_2 = 0.7; k_2 = k_1; \gamma_3 = \gamma_1; r_3 = r_1;$ $\gamma_4 = \gamma_2; r_4 = r_2; \alpha = -2; \kappa_1 = 2; \kappa_2 = 0.01;$ $a_1 = 3; a_2 = 3; a_3 = 1; a_4 = a_1; a_5 = a_2; a_6 = a_3; \xi_2 = \xi_1$

Table 2. Parameter settings of each controller for the third case.

Controller	Tuning Parameters
CHSMC	$\gamma_1 = 0.5; \gamma_3 = \gamma_1; \alpha = -2; \kappa_2 = 0.5$
HNTSMC	$\gamma_1 = 0.1; r_1 = 5/3; \gamma_3 = \gamma_1; r_3 = r_1; \alpha = -2; \kappa_1 = 0.2; \kappa_2 = 1$
HRNTSMC	$k_1 = 0.1; \gamma_1 = 0.1; r_1 = 5/3; \gamma_2 = 2; r_2 = 0.7; k_2 = k_1; \gamma_3 = \gamma_1; r_3 = r_1;$ $\gamma_4 = \gamma_2; r_4 = r_2; \alpha = -2; \kappa_1 = 0.2; \kappa_2 = 0.01;$ $a_1 = 3; a_2 = 3; a_3 = 1; a_4 = a_1; a_5 = a_2; a_6 = a_3; \xi_2 = \xi_1$

The sliding surfaces for each subsystem of the HNTSMC in [43] were defined as follows:

$$s_1(t) \triangleq e_1(t) + \gamma_1 sig(\dot{e}_1(t))^{r_1}. \tag{58}$$

$$s_2(t) \triangleq e_3(t) + \gamma_3 sig(\dot{e}_3(t))^{r_3}. \tag{59}$$

$$S(t) \triangleq \alpha s_1(t) + s_2(t). \tag{60}$$

$$\dot{S}(t) \triangleq -\kappa_1 S(t) - \kappa_2 sign(S(t)). \tag{61}$$

The sliding surfaces for each subsystem of the CHSMC [65] were defined as follows:

$$s_1(t) \triangleq e_1(t) + \gamma_1 \dot{e}_1(t). \tag{62}$$

$$s_2(t) \triangleq e_3(t) + \gamma_3 \dot{e}_3(t). \tag{63}$$

$$S(t) \triangleq \alpha s_1(t) + s_2(t). \tag{64}$$

$$\dot{S}(t) \triangleq -\kappa_2 sign(S(t)). \tag{65}$$

The CHSMC, HNTSMC, and HRNTSMC were compared in two different cases: (1) In the first case, the lumped disturbances $n_1(t)$ and $n_2(t)$ did not exist. (2) In the second case, the lumped disturbances $n_1(t)$ and $n_2(t)$ existed. (3) In the third case, besides the presence of the lumped disturbances, a substantial initial error of the angular pendulum was set, thereby emphasizing the advantages of the hierarchical sliding mode in its comparison with the other linear control methods.

Figures 4–6 show the simulation results of the three controllers in case 1. In this scenario, while the CHSMC failed to ensure the convergence of the tracking of the angular pendulum and the cart position error, the HNTSMC and HRNTSMC showcased their effectiveness in achieving this objective. In addition, the HRNTSMC demonstrated the fastest convergence speed and exhibited less oscillation near the equilibrium point, with $e_1(t) = 0$ and $e_3(t) = 0$. In the beginning, the CHSMC generated a higher cart position error $e_3(t)$ of 0.85 m, whereas the HNTSMC and HRNTSMC exhibited smaller errors, which measured 0.64 m and 0.53 m, respectively. After 40 s, both the HNTSMC and HRNTSMC performed satisfactory tracking of the angular pendulum and cart position with minimal errors. Specially, the maximum values of the steady-state tracking errors for the cart position were 0.35 m for the CHSMC, a significant improvement to 0.006 m for the HNTSMC, and an impressive reduction to just 0.001 m for the HRNTSMC. In terms of the angular pendulum errors of $e_1(t)$, the CHSMC, HNTSMC, and HRNTSMC generated the maximum steady-state errors of 0.179 rad, 0.005 rad, and 0.0005 rad, respectively. It is worth noticing that the steady-state performance outcomes of the HNTSMC and HRNTSMC significantly outperformed that of the CHSMC. Upon closer examination of the cart position and angular pendulum errors, the HRNTSMC's errors were smaller

than those of the HNTSMC. Though the HNTSMC requires higher force control than the HRNTSMC (Figure 6) and experiences more chattering in the control input, the HNTSMC still converged lower than the HRNTSMC. The convergence time of tracking the cart position error under the HRNTSMC was about 25 s, while the HNTSMC demanded about 35 s, thereby demonstrating the faster convergence speed of the HRNTSMC. The HRNTSMC can effectively alleviate chattering in the control input, use lower energy, and achieve a fast convergence speed for tracking errors. The results strongly suggest that the HRNTSMC offers better tracking performance than the CHSMC and HNTSMC. For more comprehensive qualitative analysis, Table 3 provides the index values of the integrated absolute errors (IAEs), the energy of control input (ECI), and the absolute input chattering error (AICE). These indexes are defined from [73]:

$$IAE = \frac{1}{N} \sum_{k=1}^{N} |e(k)|, \tag{66}$$

$$ECI = \frac{1}{N} \sum_{k=1}^{N} |u(k)|, \tag{67}$$

$$AICE = \frac{1}{N} \sum_{k=1}^{N} |u(k+1) - u(k)|, \tag{68}$$

where N is total number of samples, while $e(k)$ and $u(k)$ denote the position error and control input, respectively. The IAE index is responsible for qualifying tracking errors. A smaller IAE means fewer accumulated tracking errors, which in turn signifies better tracking performance. By contrast, a higher IAE implies a greater accumulation of tracking errors, thereby indicating a worse tracking capability. While the ECI is responsible for evaluating the required energy consumption, the AICE assesses the chattering in the control signal. Remarkably, the proposed controller gained the lowest index values for the IAE, ECI, and AECI. To be more specific, the IAE values of the tracking cart position in the CHSMC and HNTSMC were 0.2445 m and 0.0601 m, respectively, while only 0.00448 m was recorded value for the proposed control HRNTSMC. Similarly, when evaluating the IAE values for the tracking of the angular pendulum, the CHSMC recorded 0.1214 rad, the HNTSMC recorded 0.0381 rad, and the HRNTSMC recorded a mere 0.0217 rad. These results strongly prove the superiority of the proposed controller in terms of achieving the minimum IAE, which demonstrated fewer tracking errors compared to the CHSMC and HNTSMC. Additionally, the ECI of the proposed controller was 0.2156, thereby indicating its superior energy efficiency compared to the HNTSMC, with 0.5212, and the CHSMC, with 1.1972. In addition, the HRNTSMC significantly reduced the chattering in the control input, thus resulting in an ACEI value of 0.0605.

Table 3. Index values of control strategies in case 1.

	IAEx_1	IAEx_3	ECI	AECI
CHSMC	0.1214	0.2445	1.1972	0.3294
HNTSMC	0.0381	0.0601	0.5212	0.2814
HRNTSMC	0.0217	0.0448	0.2156	0.0605

Figures 7–11 depict the performance outcomes of the three controllers under the effects of lumped disturbances. In this context, due to the effects of the lumped disturbances, the tracking errors of the three controllers were higher compared to the first case. At the outset, the most significant error of the cart position $e_3(t)$ was recorded at 0.74 m for the CHSMC, 0.59 m for the HNTSMC, and 0.49 m for the HRNTSMC. Notably, the CHSMC produced the worst results among the three controllers despite the fact that it requires a higher control force. The three controllers performed different error convergences of the cart position and angular pendulum, as presented in Figures 7 and 8. Although the steady-state errors of the

HNTSMC and HRNTSMC were not precisely zero, they remained bounded and relatively small. The HRNTSMC stood out by providing the fastest tracking cart position and angular pendulum measurements compared to the other controllers, while still maintaining smooth force control. The effectiveness of the HRNTSMC can be attributed to its incorporation of the LESO, which can effectively estimate the lumped disturbances of the IP system with small observation errors, as are shown in Figures 10 and 11. These estimation errors of both the n_1 and n_2 came out to approximately 0.01 and 0.02, respectively. Table 4 illustrates the performance indexes of the three controllers, wherein the HRNTSMC clearly gained the smallest index values of the three controllers. As a result, this contributed to the exceptional performance of the proposed controller, which was characterized by superior tracking capability, lower energy consumption, and effective chattering reduction, even in the presence of lumped disturbances. Between the 50 s to 100 s interval, the CHSMC, HNTSMC, and HRNFTSMC controllers produced the IAE errors of 0.06 rad, 0.0023 rad, and 0.0023 rad, respectively, in tracking the angular pendulum, while they produced errors of 0.127 m, 0.0035 m, and 0.0061 m in cart position, respectively. Obviously, the HNTSMC slightly outperformed the HRNFTSMC due to the higher actuator force requirement (Figure 9) during the measurement of the steady-state errors. While the HNTSMC experienced high chattering, the HRNTSMC significantly reduced it by integrating the LESO to estimate the lumped disturbances. Table 2 provides the performance indexes of each controller, which clearly indicates that the HRNTSMC reached the lowest values of the IAE, ECI, and AECI when compared to the CHSMC and HNTSMC.

Table 4. Index values of control strategies in case 2.

	IAEx_1	**IAEx_3**	**ECI**	**AECI**
CHSMC	0.1303	0.2629	1.2877	0.3322
HNTSMC	0.0411	0.0651	0.5471	0.3117
HRNTSMC	0.0263	0.0555	0.2672	0.0629

Figures 12–14 demonstrate the performance outcomes of the three controllers under the condition of a significant initial error in the angular pendulum and the effects of lumped disturbances. In this scenario, due to the initial error of the angular pendulum, the biggest errors of the cart position were measured at 4.1 m for the CHSMC, 5 m for the HNTSMC, and 4.3 m for the HRNTSMC. Generally, despite requiring substantial control forces, the CHSMC failed to ensure the convergence errors of the angular pendulum and cart position. The tracking performance of the HNTSMC was drastically reduced, while the performance of the HRNTSMC was insignificantly affected by the initial error. Figures 12 and 13 present the different convergence errors of the three controllers. At the steady state, the HRNTSMC exhibited smaller errors in the angular pendulum compared to the HNTSMC and CHSMC, while the tracking performance of the cart position in the HRNTSMC outperformed the other controllers. Figure 14 depicts the control forces of the three controller, thus indicating that the HRNTSMC required large control input at the initial stages to balance the IP. However, the chattering problem of the HRNTSMC was significantly reduced compared to the other controllers, which became apparent after 40 s. Table 5 provides the performance indexes of the three controllers, thus showing that the HRNTSMC effectively demonstrated the smallest index values of the IAE and AECI. Despite its advantages, the ECI index value of the HRNTSMC was slightly higher than the HNTSMC, which is attributed to the large control force at the initial stage from 20 s. As a result, the proposed controller demonstrates effective performance of the IP in the case of a large initial error of the angular pendulum.

Table 5. Index values of control strategies in case 3.

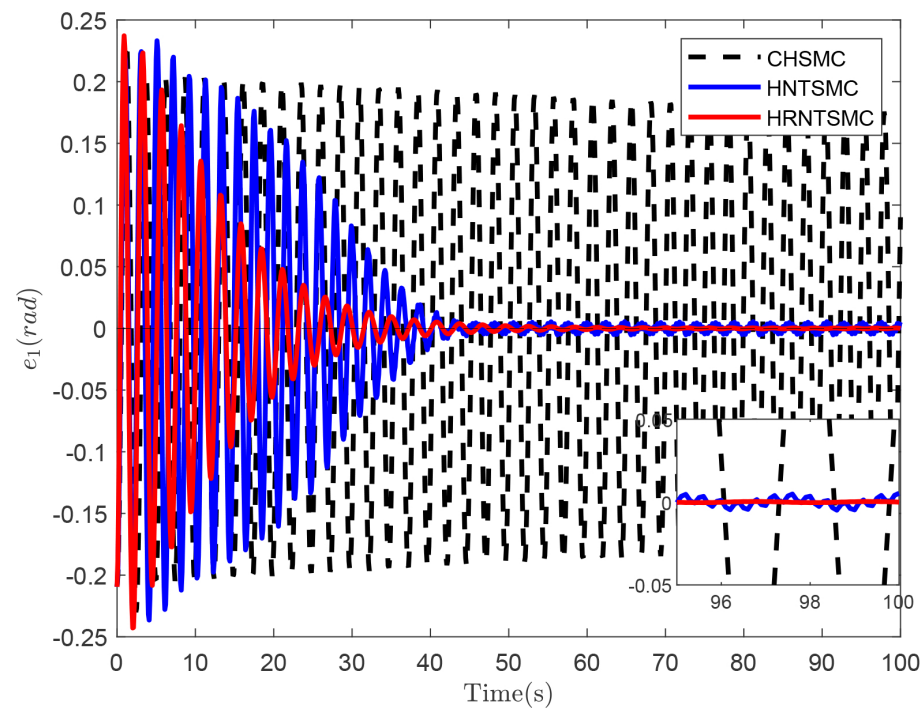|	**IAEx_1**	**IAEx_3**	**ECI**	**AECI**
CHSMC	0.6058	1.2271	9.2318	4.0046
HNTSMC	0.0807	0.8674	0.9029	0.6959
HRNTSMC	0.0746	0.1816	1.0154	0.4238

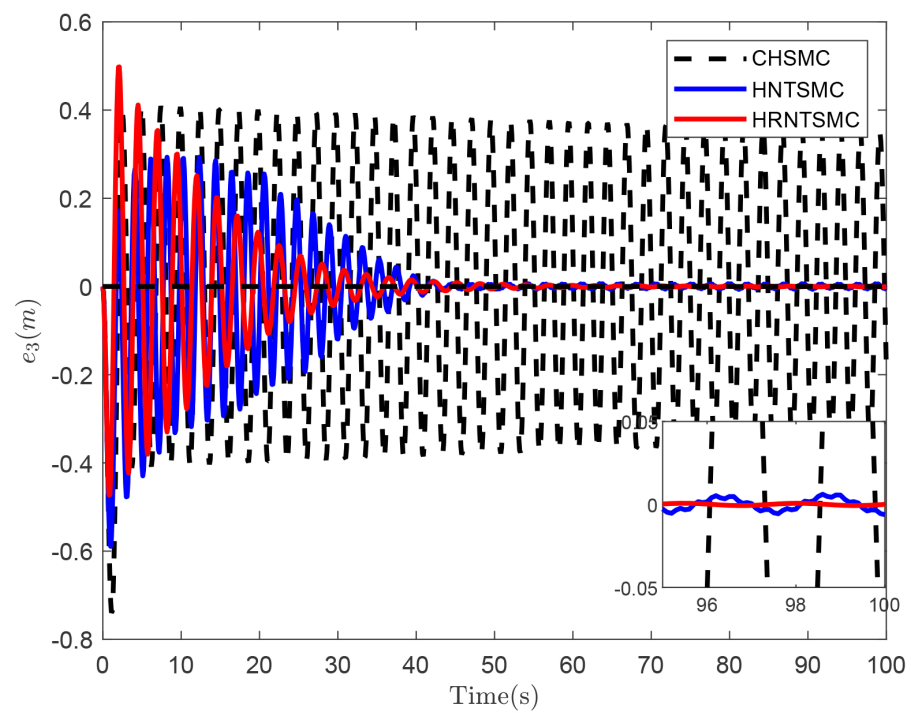**Figure 4.** The error convergence of angular pendulum in case 1.

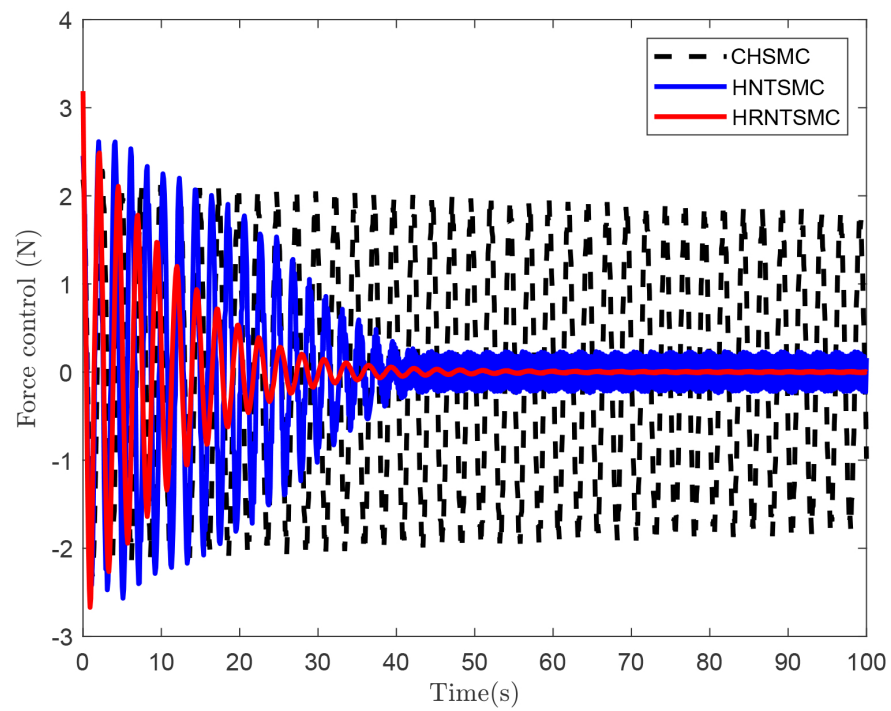**Figure 5.** The error convergence of cart position in case 1.

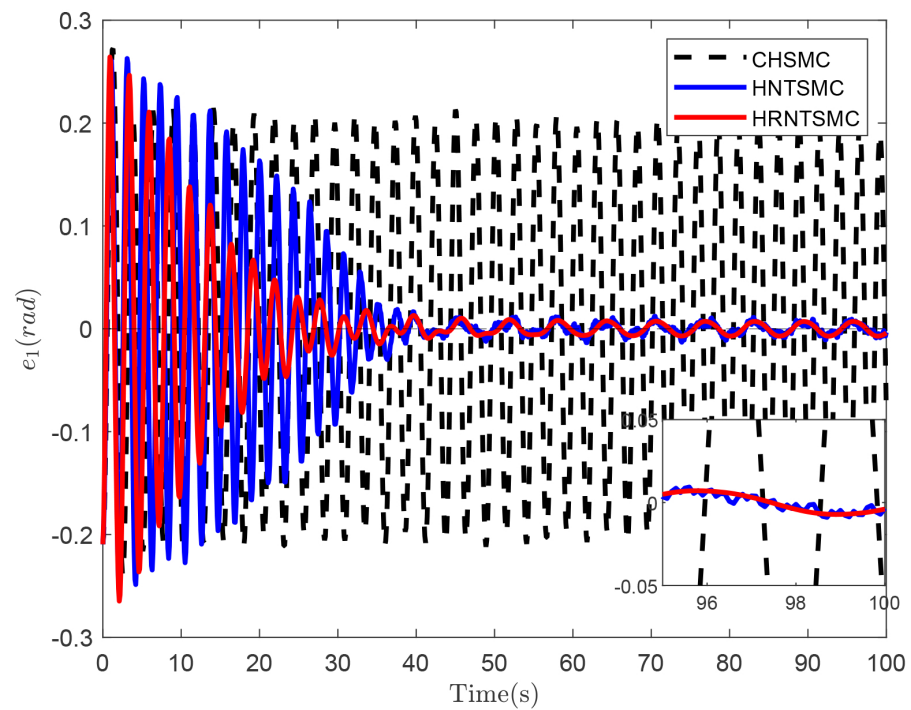**Figure 6.** Force control in case 1.

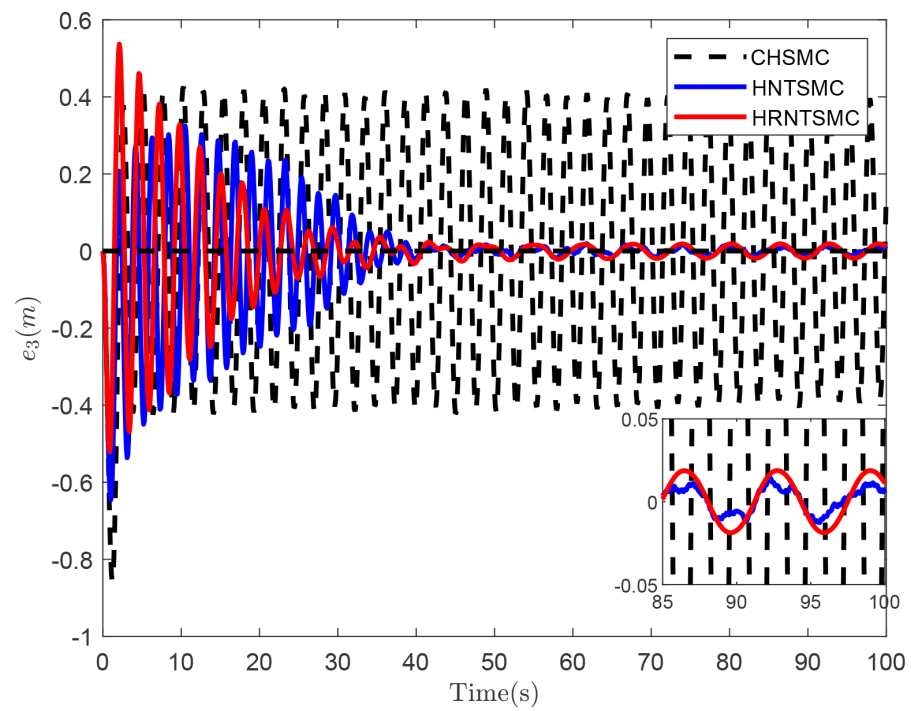**Figure 7.** The error convergence of angular pendulum in case 2.

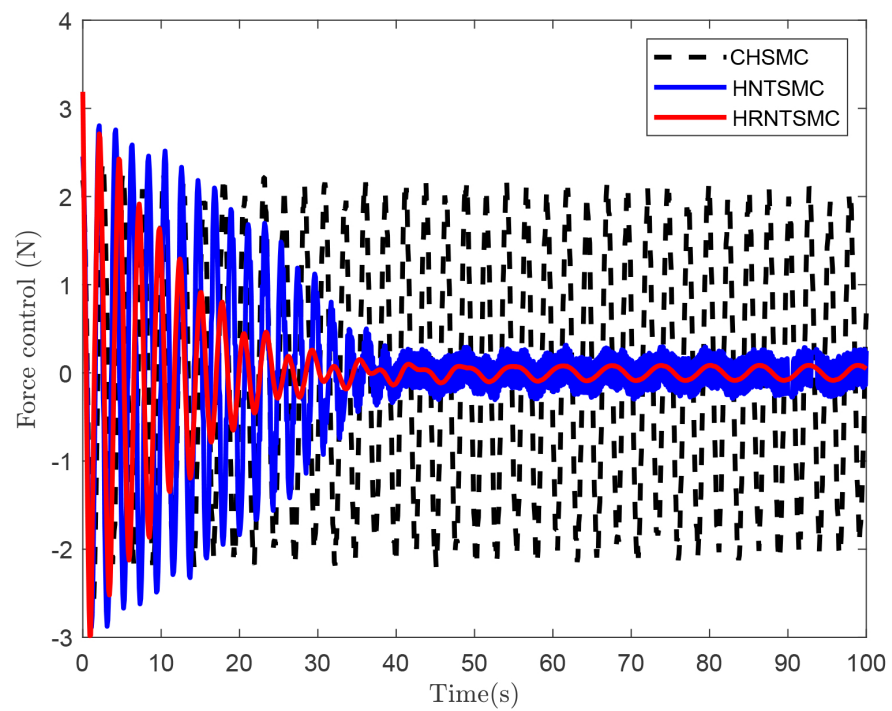**Figure 8.** The error convergence of cart position in case 2.
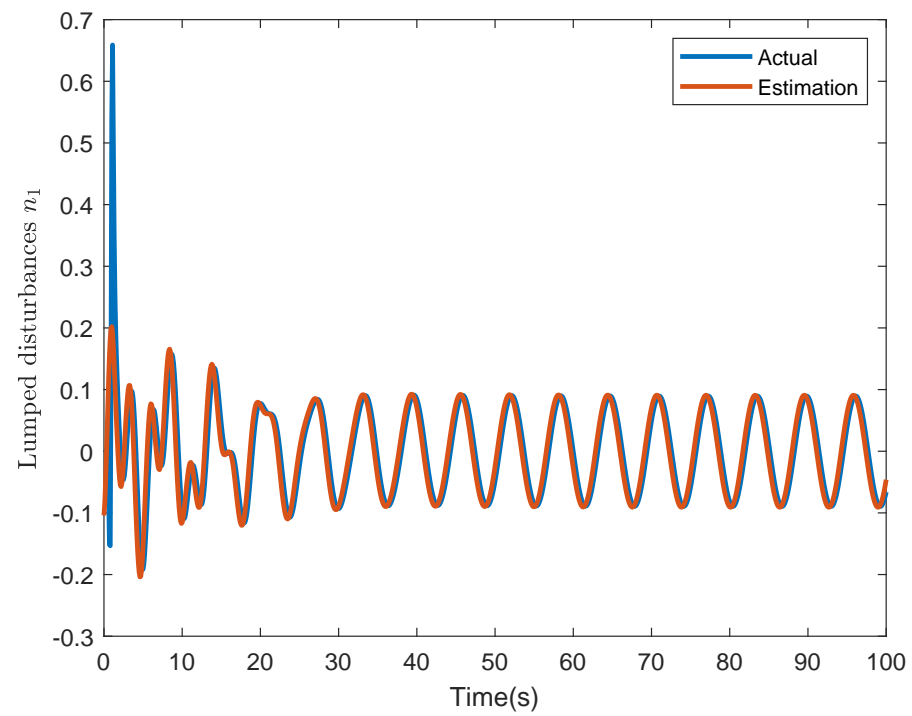

Figure 9. Force control in case 2.

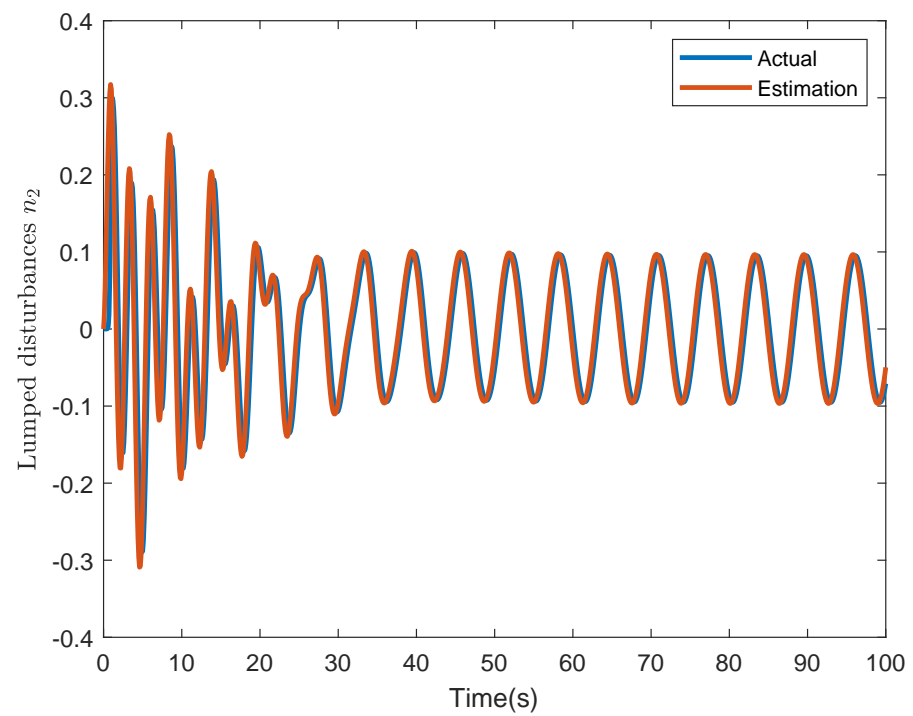**Figure 10.** The estimated values of lumped disturbances n_1.

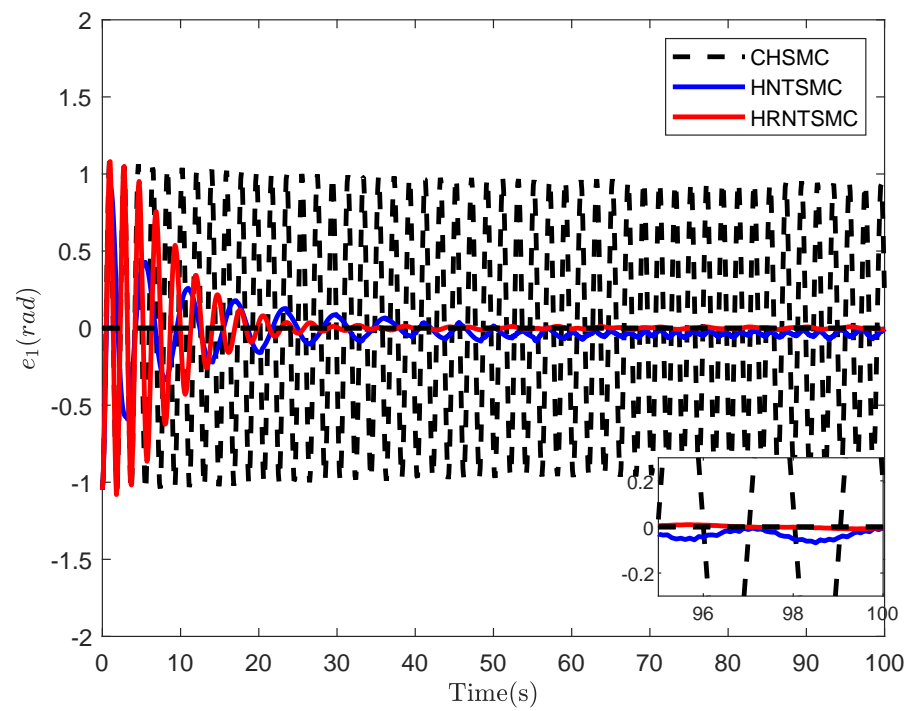**Figure 11.** The estimated values of lumped disturbances n_2.

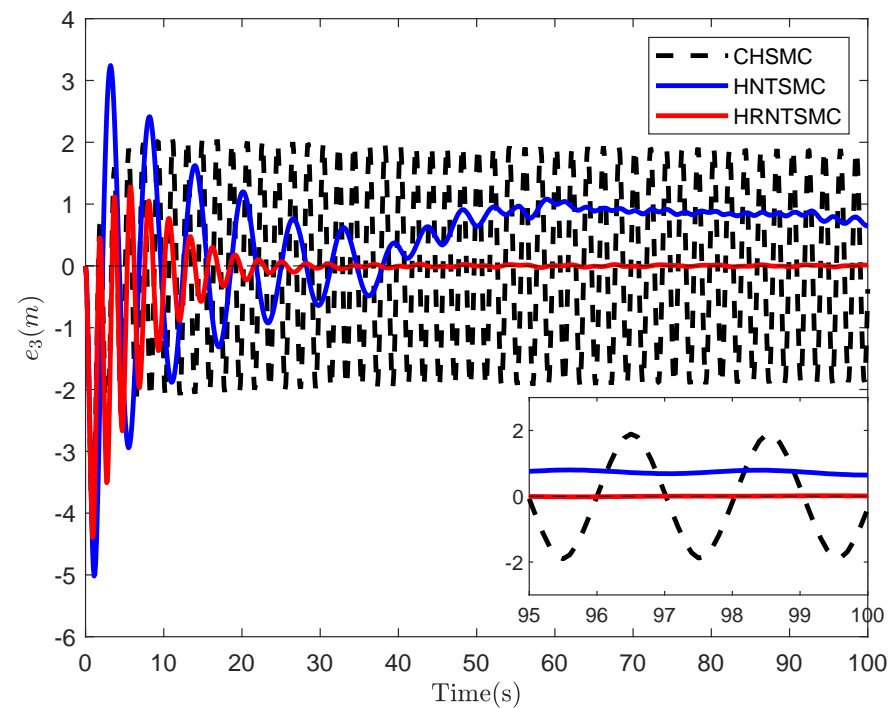**Figure 12.** The error convergence of angular pendulum in case 3.

Figure 13. The error convergence of cart position in case 3.
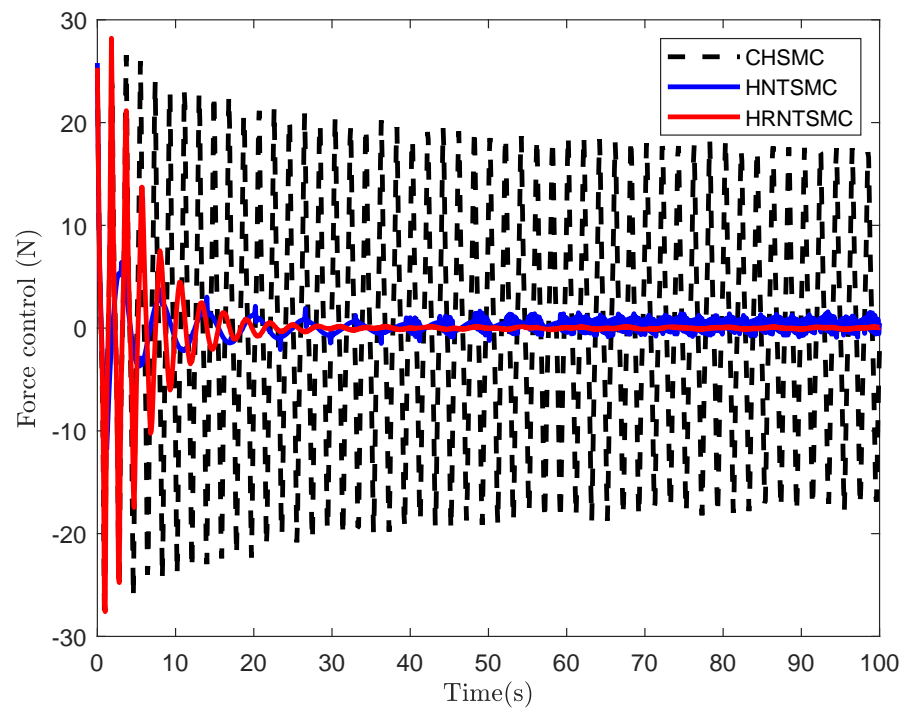
Figure 14. Force control in case 3.

5. Conclusions

This work proposes the HRNTSMC as an effective approach to increase convergence speed and reduce control input chattering in the IP system. Throughout this study, the simulation results confirm the applicability and performance of the proposed controller. Despite outperforming other compared controllers, it is acknowledged that the proposed controller contains more parameters for tuning, which could be determined using optimization methods in future work. However, it is essential to note that the present work is limited to a simulation-based investigation, which is aimed at showing the feasibility of this approach and establishing a theoretical foundation. Hence, to verify the practical implementation of the proposed controller in real-world scenarios, the next phase should involve experimental work.

Author Contributions: Conceptualization, H.D.L.; Methodology, H.D.L.; Software, H.D.L.; Validation, H.D.L.; Formal analysis, H.D.L.; Investigation, H.D.L.; Writing—original draft, H.D.L.; Writing—review and editing, T.N.; Visualization, H.D.L. and T.N.; Supervision, T.N.; Funding acquisition, T.N. All authors have read and agreed to the published version of the manuscript.

Data Availability Statement: The authors are willing to share data with interested researchers upon request.

Conflicts of Interest: The authors declare that they have no known competing financial interests or personal relationships that could have appeared to influence the work reported in this paper.

Appendix A. Stability of the LESO

We define the scaled estimation error vector of the LESO as follows:

$$\mathbf{v}(t) \triangleq [v_1(t), v_2(t), v_3(t)]^T \triangleq [\frac{x_1(t) - \hat{x}_1(t)}{\xi_1^2}, \frac{x_2(t) - \hat{x}_2(t)}{\xi_1}, n_1(t) - \hat{n}_1(t)]. \qquad (A1)$$

By combining (1), (2), and (32)–(34), we obtain the following:

$$\xi_1 \dot{v}_1(t) = \frac{\dot{x}_1(t) - \dot{\hat{x}}_1(t)}{\xi_1(t)} = -a_1 v_1(t) + v_2(t). \tag{A2}$$

$$\xi_1 \dot{v}_2(t) = \dot{x}_2(t) - \dot{\hat{x}}_2(t) = -a_2 v_1(t) + v_3(t). \tag{A3}$$

$$\xi_1 \dot{v}_3(t) = \dot{n}_1(t) - \dot{\hat{n}}(t) = -a_3 v_1(t) + \xi_1 \dot{n}_1(t). \tag{A4}$$

The estimation error dynamics equation can be rewritten as follows:

$$\xi_1 \dot{\mathbf{v}}(t) = \mathbf{A}\mathbf{v}(t) + \xi_1 \mathbf{B}\dot{n}_1(t), \tag{A5}$$

where

$$\mathbf{A} = \begin{bmatrix} -a_1 & 1 & 0 \\ -a_2 & 0 & 1 \\ -a_3 & 0 & 0 \end{bmatrix}; \tag{A6}$$

$$\mathbf{B} = \begin{bmatrix} 0 \\ 0 \\ 1 \end{bmatrix}; \tag{A7}$$

The characteristic equation of matrix A is defined as follows:

$$|\lambda \mathbf{I} - \mathbf{A}| = \begin{bmatrix} \lambda + a_1 & -1 & 0 \\ a_2 & \lambda & -1 \\ a_3 & 0 & \lambda \end{bmatrix} = 0. \tag{A8}$$

Then,

$$(\lambda + a_1)\lambda^2 + a_2\lambda + a_3 = 0. \tag{A9}$$

And,

$$\lambda^3 + a_1\lambda^2 + a_2\lambda + a_3 = 0. \tag{A10}$$

By choosing suitable values for a_1, a_2, and a_3, we can make $\mathbf{A}$ a Hurwitz matrix, which has the real part of its eigenvalues being negative. For any given three-dimensional symmetric positive definite matrix $\mathbf{Q}$, there exists a symmetric positive definite matrix $\mathbf{P}$, which satisfies the following condition:

$$\mathbf{A}^{\mathbf{T}}\mathbf{P} + \mathbf{P}\mathbf{A} + \mathbf{Q} = 0. \tag{A11}$$

The Lyapunov function of the LESO is defined as follows:

$$V_e(t) \triangleq \xi_1 \mathbf{v}(t)^T \mathbf{P}\mathbf{v}(t). \tag{A12}$$

The time derivative of $V_e(t)$ is defined as follows:

$$\dot{V}_e(t) = \xi_1 \dot{\mathbf{v}}(t)^T \mathbf{P}\mathbf{v}(t) + \xi_1 \mathbf{v}(t)^T \mathbf{P}\dot{\mathbf{v}}(t). \tag{A13}$$

$$\dot{V}_e(t) = (\mathbf{A}\mathbf{v}(t) + \xi_1 \mathbf{B}\dot{n}_1)^T \mathbf{P}\mathbf{v}(t) + \xi_1 \mathbf{v}(t)^T \mathbf{P}(\mathbf{A}\mathbf{v}(t) + \xi_1 \mathbf{B}\dot{n}_1(t)). \tag{A14}$$

$$\dot{V}_e(t) = \mathbf{v}(t)^T (\mathbf{A}^T \mathbf{P} + \mathbf{P}\mathbf{A})\mathbf{v}(t) + 2\xi_1 \mathbf{v}(t)^T \mathbf{P}\mathbf{B}\dot{n}_1(t). \tag{A15}$$

$$\dot{V}_e(t) \leq -\mathbf{v}^T \mathbf{Q}\mathbf{v} + 2\xi_1 ||\mathbf{P}\mathbf{B}|| \cdot |\mathbf{v}(t)| \cdot |\dot{n}_1(t)|. \tag{A16}$$

We assume that $|\dot{n}_1(t)| \leq L$; then:

$$\dot{V}_e(t) \leq -\lambda_{min}(\mathbf{Q})||\mathbf{v}(t)||^2 + 2\bar{\xi}_1||\mathbf{PB}|| \cdot |\mathbf{v}(t)| \cdot |L|, \tag{A17}$$

where $\lambda_{min}(\mathbf{Q})$ is the minimum eigenvalue of $\mathbf{Q}$, where $\dot{V}_e(t) \leq 0$; the observer error convergence is defined as follows:

$$||\mathbf{v}(t)|| \leq \frac{2\bar{\xi}_1||\mathbf{PB}|| \cdot |L|}{\lambda_{min}(\mathbf{Q})}. \tag{A18}$$

To simplify the complexity of the LESO, matrix $\mathbf{Q}$ is selected as the identity matrix $\mathbf{I}$ [74], and the polynomial (A10) is selected based on [75]:

$$\lambda^3 + a_1\lambda^2 + a_2\lambda + a_3 = (s + \omega)^3, \tag{A19}$$

where ω presents the bandwidth of the LESO. It can be seen that the observer error depends on the bound of the derivative disturbance $|L|$ and $||\mathbf{PB}||$. The value of $||\mathbf{PB}||$ is influenced by the eigenvalues of the matrix $\mathbf{A}$, as $\mathbf{P}$ is determined by (A11), with $\mathbf{Q}$ being the identity matrix. To enhance the accuracy of the disturbances estimation, selecting a large ω value results in a small value of $||\mathbf{PB}||$. However, in a practical system, ω is limited by the bandwidth of the controller and the sampling frequency of the system [57]. When the high-frequency disturbances exist in the IP system, the LESO requires maximum ω values to achieve the fast convergence of estimation, which can introduce more noise and diminish the observer performance. Addressing this challenge will be a focus of the future work.

References

1. Irfan, S.; Mehmood, A.; Razzaq, M.T.; Iqbal, J. Advanced sliding mode control techniques for inverted pendulum: Modelling and simulation. *Eng. Sci. Technol. Int. J.* **2018**, *21*, 753–759. [CrossRef]
2. Kim, S.; Kwon, S. Nonlinear optimal control design for underactuated two-wheeled inverted pendulum mobile platform. *IEEE/ASME Trans. Mechatronics* **2017**, *22*, 2803–2808. [CrossRef]
3. Sentis, L. Compliant control of whole-body multi-contact behaviors in humanoid robots. In *Motion Planning for Humanoid Robots*; Springer: Berlin/Heidelberg, Germany, 2010; pp. 29–66.
4. Wang, W.; Yi, J.; Zhao, D.; Liu, D. Design of a stable sliding-mode controller for a class of second-order underactuated systems. *IEE Proc. -Control Theory Appl.* **2004**, *151*, 683–690. [CrossRef]
5. Horibe, T.; Sakamoto, N. Optimal swing up and stabilization control for inverted pendulum via stable manifold method. *IEEE Trans. Control. Syst. Technol.* **2017**, *26*, 708–715. [CrossRef]
6. Ismail, N. Fuzzy Logic Controller Design for Inverted Pendulum System. Ph.D. Thesis, Universiti Tun Hussein Malaysia, Johor, Malaysia, 2013.
7. Bennett, S. Development of the PID controller. *IEEE Control Syst. Mag.* **1993**, *13*, 58–62.
8. Ghosh, A.; Krishnan, T.; Subudhi, B. Robust proportional–integral–derivative compensation of an inverted cart–pendulum system: An experimental study. *IET Control Theory Appl.* **2012**, *6*, 1145–1152. [CrossRef]
9. Batista, J.G.; Souza, D.A.; dos Reis, L.L.; Filgueiras, L.V.; Ramos, K.M.; Junior, A.B.; Correia, W.B. Performance comparison between the PID and LQR controllers applied to a robotic manipulator joint. In Proceedings of the IECON 2019-45th Annual Conference of the IEEE Industrial Electronics Society, Lisbon, Portugal, 14–17 October 2019; Volume 1, pp. 479–484.
10. Wang, H.; Dong, H.; He, L.; Shi, Y.; Zhang, Y. Design and simulation of LQR controller with the linear inverted pendulum. In Proceedings of the 2010 International Conference on Electrical and Control Engineering, Wuhan, China, 25–27 June 2010; pp. 699–702.
11. Camacho, O.; Smith, C.A. Sliding mode control: An approach to regulate nonlinear chemical processes. *ISA Trans.* **2000**, *39*, 205–218. [CrossRef]
12. Huang, C.H.; Wang, W.J.; Chiu, C.H. Design and implementation of fuzzy control on a two-wheel inverted pendulum. *IEEE Trans. Ind. Electron.* **2010**, *58*, 2988–3001. [CrossRef]
13. Yang, C.; Li, Z.; Cui, R.; Xu, B. Neural network-based motion control of an underactuated wheeled inverted pendulum model. *IEEE Trans. Neural Netw. Learn. Syst.* **2014**, *25*, 2004–2016. [CrossRef]
14. Shtessel, Y.; Edwards, C.; Fridman, L.; Levant, A. *Sliding Mode Control and Observation*; Springer: Berlin/Heidelberg, Germany, 2014; Volume 10.
15. Krafes, S.; Chalh, Z.; Saka, A. Linear, nonlinear and intelligent controllers for the inverted pendulum problem. In Proceedings of the 2016 International Conference on Electrical and Information Technologies (ICEIT), Tangiers, Morocco, 4–7 May 2016; pp. 136–141.

16. Utkin, V.I. Sliding mode control in discrete-time and difference systems. In *Variable Structure and Lyapunov Control*; Springer: Berlin/Heidelberg, Germany, 2005; pp. 87–107.

17. Utkin, V.I. *Sliding Modes in Control and Optimization*; Springer Science & Business Media: Berlin/Heidelberg, Germany, 2013.

18. Basin, M.V.; Yu, P.; Shtessel, Y.B. Hypersonic missile adaptive sliding mode control using finite-and fixed-time observers. *IEEE Trans. Ind. Electron.* **2017**, *65*, 930–941. [CrossRef]

19. Wang, G.; Xu, Q. Design and precision position/force control of a piezo-driven microinjection system. *IEEE/ASME Trans. Mechatronics* **2017**, *22*, 1744–1754. [CrossRef]

20. Liu, Y.; Zhang, Y.; Xu, Q. Design and control of a novel compliant constant-force gripper based on buckled fixed-guided beams. *IEEE/ASME Trans. Mechatronics* **2016**, *22*, 476–486. [CrossRef]

21. Zhihong, M.; Paplinski, A.P.; Wu, H.R. A robust MIMO terminal sliding mode control scheme for rigid robotic manipulators. *IEEE Trans. Autom. control* **1994**, *39*, 2464–2469. [CrossRef]

22. Yu, X.; Zhihong, M. Fast terminal sliding-mode control design for nonlinear dynamical systems. *IEEE Trans. Circuits Syst. I Fundam. Theory Appl.* **2002**, *49*, 261–264.

23. Feng, Y.; Yu, X.; Man, Z. Non-singular terminal sliding mode control of rigid manipulators. *Automatica* **2002**, *38*, 2159–2167. [CrossRef]

24. Shao, K.; Zheng, J.; Huang, K.; Wang, H.; Man, Z.; Fu, M. Finite-time control of a linear motor positioner using adaptive recursive terminal sliding mode. *IEEE Trans. Ind. Electron.* **2019**, *67*, 6659–6668. [CrossRef]

25. Utkin, V.; Lee, H. Chattering problem in sliding mode control systems. In Proceedings of the International Workshop on Variable Structure Systems, 2006. VSS'06, Alghero, Sardinia, 5–7 June 2006; pp. 346–350.

26. Asad, M.; Bhatti, A.I.; Iqbal, S. A novel reaching law for smooth sliding mode control using inverse hyperbolic function. In Proceedings of the 2012 International Conference on Emerging Technologies, Islamabad, Pakistan, 8–9 October 2012; pp. 1–6.

27. Le, H.D.; Nestorović, T. Adaptive Proportional Integral Derivative Nonsingular Dual Terminal Sliding Mode Control for Robotic Manipulators. *Dynamics* **2023**, *3*, 656–677. [CrossRef]

28. Kim, K.S.; Rew, K.H.; Kim, S. Disturbance observer for estimating higher order disturbances in time series expansion. *IEEE Trans. Autom. control* **2010**, *55*, 1905–1911.

29. Zhang, J.; Liu, X.; Xia, Y.; Zuo, Z.; Wang, Y. Disturbance observer-based integral sliding-mode control for systems with mismatched disturbances. *IEEE Trans. Ind. Electron.* **2016**, *63*, 7040–7048. [CrossRef]

30. Mobayen, S.; Tchier, F. Nonsingular fast terminal sliding-mode stabilizer for a class of uncertain nonlinear systems based on disturbance observer. *Sci. Iran.* **2017**, *24*, 1410–1418. [CrossRef]

31. Chen, W.H.; Yang, J.; Guo, L.; Li, S. Disturbance-observer-based control and related methods—An overview. *IEEE Trans. Ind. Electron.* **2015**, *63*, 1083–1095. [CrossRef]

32. Guo, B.Z.; Zhao, Z.L. Extended state observer for nonlinear systems with uncertainty. *IFAC Proc. Vol.* **2011**, *44*, 1855–1860. [CrossRef]

33. Liu, Y.C.; Laghrouche, S.; Depernet, D.; N'Diaye, A.; Djerdir, A.; Cirrincione, M. Super-twisting sliding-mode observer-based model reference adaptive speed control for PMSM drives. *J. Frankl. Inst.* **2023**, *360*, 985–1004. [CrossRef]

34. Zhang, J.; Gao, W.; Guo, Q. Extended State Observer-Based Sliding Mode Control Design of Two-DOF Lower Limb Exoskeleton. *Actuators* **2023**, *12*, 402. [CrossRef]

35. Chen, H.; Sun, N. Nonlinear control of underactuated systems subject to both actuated and unactuated state constraints with experimental verification. *IEEE Trans. Ind. Electron.* **2019**, *67*, 7702–7714. [CrossRef]

36. Utkin, V.; Guldner, J.; Shi, J. *Sliding Mode Control in Electro-Mechanical Systems*; CRC Press: Boca Raton, FL, USA, 2017.

37. Idrees, M.; Muhammad, S.; Ullah, S. Robust hierarchical sliding mode control with state-dependent switching gain for stabilization of rotary inverted pendulum. *Kybernetika* **2019**, *55*, 455–471. [CrossRef]

38. Zhao, H.; Zong, G.; Zhao, X.; Wang, H.; Xu, N.; Zhao, N. Hierarchical Sliding-Mode Surface-Based Adaptive Critic Tracking Control for Nonlinear Multiplayer Zero-Sum Games Via Generalized Fuzzy Hyperbolic Models. *IEEE Trans. Fuzzy Syst.* **2023**, *31*, 4010–4023. [CrossRef]

39. Hwang, C.L.; Chiang, C.C.; Yeh, Y.W. Adaptive fuzzy hierarchical sliding-mode control for the trajectory tracking of uncertain underactuated nonlinear dynamic systems. *IEEE Trans. Fuzzy Syst.* **2013**, *22*, 286–299. [CrossRef]

40. Hwang, C.L.; Wu, H.M. Trajectory tracking of a mobile robot with frictions and uncertainties using hierarchical sliding-mode under-actuated control. *IET Control Theory Appl.* **2013**, *7*, 952–965. [CrossRef]

41. Nafa, F.; Labiod, S.; Chekireb, H. A structured sliding mode controller for a class of underactuated mechanical systems. In Proceedings of the International Workshop on Systems, Signal Processing and their Applications, WOSSPA, Tipaza, Algeria, 9–11 May 2011; pp. 243–246.

42. Yue, S.; Niu, B.; Wang, H.; Zhang, L.; Ahmad, A.M. Hierarchical sliding mode-based adaptive fuzzy control for uncertain switched under-actuated nonlinear systems with input saturation and dead-zone. *Robot. Intell. Autom.* **2023**, *43*, 523–536. [CrossRef]

43. Min-xiu, Y.; Yuan-wei, J. Terminal sliding mode decomposed control for a class of nonlinear systems. In Proceedings of the 2008 Chinese Control and Decision Conference, Yantai, China, 2–4 July 2008; pp. 4988–4991.

44. Bayramoglu, H.; Komurcugil, H. Nonsingular decoupled terminal sliding-mode control for a class of fourth-order nonlinear systems. *Commun. Nonlinear Sci. Numer. Simul.* **2013**, *18*, 2527–2539. [CrossRef]

45. Edwards, C.; Shtessel, Y.B. Adaptive continuous higher order sliding mode control. *Automatica* **2016**, *65*, 183–190. [CrossRef]

46. Wang, H.; Li, Z.; Jin, X.; Huang, Y.; Kong, H.; Yu, M.; Ping, Z.; Sun, Z. Adaptive integral terminal sliding mode control for automobile electronic throttle via an uncertainty observer and experimental validation. *IEEE Trans. Veh. Technol.* **2018**, *67*, 8129–8143. [CrossRef]

47. Liu, W.; Chen, S.; Huang, H. Actor-Critic learning hierarchical sliding mode control for a class of underactuated systems. In Proceedings of the 2019 Chinese Automation Congress (CAC), Hangzhou, China, 22–24 November 2019; pp. 1–6.

48. Li, S.; Yang, J.; Chen, W.H.; Chen, X. Generalized extended state observer based control for systems with mismatched uncertainties. *IEEE Trans. Ind. Electron.* **2011**, *59*, 4792–4802. [CrossRef]

49. Czyżniewski, M.; Łangowski, R.; Klassa, D.; Matwiszyn, M. A case study of robust sliding mode control applied to inverted pendulum on a cart. In Proceedings of the 2021 25th International Conference on Methods and Models in Automation and Robotics (MMAR), Miedzyzdroje, Poland, 23–26 August 2021; pp. 156–161.

50. Haimo, V.T. Finite time controllers. *SIAM J. Control Optim.* **1986**, *24*, 760–770. [CrossRef]

51. Qian, D.; Yi, J.; Zhao, D.; Hao, Y. Hierarchical sliding mode control for series double inverted pendulums system. In Proceedings of the 2006 IEEE/RSJ International Conference on Intelligent Robots and Systems, Beijing, China, 9–15 October 2006; pp. 4977–4982.

52. Chiu, C.S. Derivative and integral terminal sliding mode control for a class of MIMO nonlinear systems. *Automatica* **2012**, *48*, 316–326. [CrossRef]

53. Bartoszewicz, A. A new reaching law for sliding mode control of continuous time systems with constraints. *Trans. Inst. Meas. Control* **2015**, *37*, 515–521. [CrossRef]

54. Yue, M.; Liu, B. Adaptive control of an underactuated spherical robot with a dynamic stable equilibrium point using hierarchical sliding mode approach. *Int. J. Adapt. Control Signal Process.* **2014**, *28*, 523–535. [CrossRef]

55. Qian, D.; Yi, J.; Zhao, D. Multiple layers sliding mode control for a class of under-actuated systems. In Proceedings of the Multiconference on Computational Engineering in Systems Applications, Beijing, China, 4–6 October 2006; Volume 1, pp. 530–535.

56. Wang, H.; Shi, L.; Man, Z.; Zheng, J.; Li, S.; Yu, M.; Jiang, C.; Kong, H.; Cao, Z. Continuous fast nonsingular terminal sliding mode control of automotive electronic throttle systems using finite-time exact observer. *IEEE Trans. Ind. Electron.* **2018**, *65*, 7160–7172. [CrossRef]

57. Gao, Z. Scaling and bandwidth-parameterization based controller tuning. In Proceedings of the ACC, Denver, CO, USA, 4–6 June 2003; pp. 4989–4996.

58. Sussmann, H.; Kokotovic, P. The peaking phenomenon and the global stabilization of nonlinear systems. *IEEE Trans. Autom. Control* **1991**, *36*, 424–440. [CrossRef]

59. Huang, Y.; Han, J. Analysis and design for the second order nonlinear continuous extended states observer. *Chin. Sci. Bull.* **2000**, *45*, 1938–1944. [CrossRef]

60. Wang, J.; Wu, Y.; Dong, X. Recursive terminal sliding mode control for hypersonic flight vehicle with sliding mode disturbance observer. *Nonlinear Dyn.* **2015**, *81*, 1489–1510. [CrossRef]

61. Shi, S.L.; Li, J.X.; Fang, Y.M. Extended-state-observer-based chattering free sliding mode control for nonlinear systems with mismatched disturbance. *IEEE Access* **2018**, *6*, 22952–22957. [CrossRef]

62. González, I.; Salazar, S.; Lozano, R. Chattering-free sliding mode altitude control for a quad-rotor aircraft: Real-time application. *J. Intell. Robot. Syst.* **2014**, *73*, 137–155. [CrossRef]

63. Liu, Q.; Lv, Z.; Wu, Y. Design of sliding mode controller based on high-gain observer of inverted pendulum on a cart. In Proceedings of the 2019 Chinese Control Conference (CCC), Guangzhou, China, 27–30 July 2019; pp. 846–851.

64. Cui, M.; Liu, W.; Liu, H.; Jiang, H.; Wang, Z. Extended state observer-based adaptive sliding mode control of differential-driving mobile robot with uncertainties. *Nonlinear Dyn.* **2016**, *83*, 667–683. [CrossRef]

65. Muhammad, S.; Idrees, M. Comparative study of hierarchical sliding mode control and decoupled sliding mode control. In Proceedings of the 2017 12th IEEE Conference on Industrial Electronics and Applications (ICIEA), Siem Reap, Cambodia, 18–20 June 2017; pp. 818–824.

66. Guo, B.; Bacha, S.; Alamir, M.; Hably, A.; Boudinet, C. Generalized integrator-extended state observer with applications to grid-connected converters in the presence of disturbances. *IEEE Trans. Control Syst. Technol.* **2020**, *29*, 744–755. [CrossRef]

67. Mahmoodabadi, M.J.; Khoobroo Haghbayan, H. An optimal adaptive hybrid controller for a fourth-order under-actuated nonlinear inverted pendulum system. *Trans. Inst. Meas. Control* **2020**, *42*, 285–294. [CrossRef]

68. Haghighi, D.A.; Mobayen, S. Design of an adaptive super-twisting decoupled terminal sliding mode control scheme for a class of fourth-order systems. *ISA Trans.* **2018**, *75*, 216–225. [CrossRef] [PubMed]

69. Boukattaya, M.; Gassara, H.; Damak, T. A global time-varying sliding-mode control for the tracking problem of uncertain dynamical systems. *ISA Trans.* **2020**, *97*, 155–170. [CrossRef] [PubMed]

70. Mei, K.; Ding, S. Second-order sliding mode controller design subject to an upper-triangular structure. *IEEE Trans. Syst. Man Cybern. Syst.* **2018**, *51*, 497–507. [CrossRef]

71. Qiao, L.; Zhang, W. Trajectory tracking control of AUVs via adaptive fast nonsingular integral terminal sliding mode control. *IEEE Trans. Ind. Inform.* **2019**, *16*, 1248–1258. [CrossRef]

72. Yao, Q. Adaptive finite-time sliding mode control design for finite-time fault-tolerant trajectory tracking of marine vehicles with input saturation. *J. Frankl. Inst.* **2020**, *357*, 13593–13619. [CrossRef]

73. Sai, H.; Xu, Z.; He, S.; Zhang, E.; Zhu, L. Adaptive nonsingular fixed-time sliding mode control for uncertain robotic manipulators under actuator saturation. *ISA Trans.* **2022**, *123*, 46–60. [CrossRef] [PubMed]

74. Li, H.; Yang, S.; Kong, L.; Wen, T. High-precision angular speed tracking control of gimbal system with harmonic reducer. *IEEE Trans. Ind. Electron.* **2021**, *69*, 8168–8177. [CrossRef]

75. Lau, J.Y.; Liang, W.; Tan, K.K. Motion control for piezoelectric-actuator-based surgical device using neural network and extended state observer. *IEEE Trans. Ind. Electron.* **2019**, *67*, 402–412. [CrossRef]